Global anthropogenic aerosol direct forcing derived from satellite and ground-based observations

Chul Eddy Chung, V. Ramanathan, Dohyeong Kim, and I. A. Podgorny
Center for Clouds, Chemistry, and Climate (C^4), Scripps Institution of Oceanography, La Jolla, California, USA

Received 11 June 2005; revised 6 October 2005; accepted 20 October 2005; published 23 December 2005.

[1] A global estimate of the direct effects of anthropogenic aerosols on solar radiation in cloudy skies is obtained by integrating satellite and ground-based observations with models of aerosol chemistry, transport, and radiative transfer. The models adopt global distribution of aerosol optical depths (from MODIS), clouds, water vapor, ozone, and surface albedo from various satellite climatology. Gaps and errors in satellite derived aerosol optical depths are filled and corrected by surface network (AERONET), and an aerosol chemical-transport model (GOCART) by using statistical techniques. Using these derived aerosol properties and other related variables, we generate climatological monthly mean anthropogenic aerosol forcing for both clear and average cloudy skies. Unless otherwise stated, our estimates are for average cloudy skies, also referred to as all sky conditions. The global annual mean direct forcing is -0.35 Wm^{-2} (range of -0.6 to -0.1 Wm^{-2}) at the top-of-the atmosphere (TOA), $+3.0$ Wm^{-2} (range of $+2.7$ to $+3.3Wm^{-2}$) in the atmosphere, and -3.4 Wm^{-2} (range of -3.5 to -3.3 Wm^{-2}) at the surface. The uncertainty of about 10–20% in the surface and atmosphere forcing translates into a six fold uncertainty in the TOA forcing because the TOA forcing is a small sum of two large terms (surface and atmosphere) of opposing signs. Given the current state of observations and modeling, it is very difficult to further reduce the uncertainty in the estimated TOA forcing. The major contributors to the uncertainty in atmospheric absorption are from the uncertainty in the vertical distribution of aerosols and the single scattering albedo of aerosols. The TOA forcing in clear skies is a factor of two different, while the surface and atmosphere forcing terms differ by only about 10–25%. Another major finding of this study is that the reduction in the surface solar radiation is a factor of 10 larger than the reduction in net solar (down minus up) radiation at TOA. The TOA forcing changes sign regionally, whereas the surface forcing is always negative. Thus caution must be exercised against relying too strongly on assessing the aerosol impacts based solely on global mean forcing. Aerosols over the NH contribute about 64% to the global surface forcing. Regionally the populated tropical regions contribute the most to the global surface forcing, with Asia the largest contributor. Roughly 49% of the total surface forcing is over the oceanic regions. Most of the previous global aerosol forcing estimate studies were conducted with a chemical transport model coupled to a general circulation model with model generated aerosols and cloudiness. Thus the present study, which adopts observed aerosol properties and observed three dimensional cloudiness, provides an independent approach for estimating the aerosol forcing.

Citation: Chung, C. E., V. Ramanathan, D. Kim, and I. A. Podgorny (2005), Global anthropogenic aerosol direct forcing derived from satellite and ground-based observations, *J. Geophys. Res.*, *110*, D24207, doi:10.1029/2005JD006356.

1. Introduction

[2] Aerosol radiative forcing is defined as the effect of aerosol, both natural and anthropogenic, on the radiative fluxes at the top of the atmosphere (TOA) and at the surface and on the absorption of radiation within the atmosphere. The direct effect of aerosols on radiation, i.e., direct radiative forcing (DRF), has been estimated globally by several studies [e.g., *Penner et al.*, 1992; *Hansen et al.*, 2002] (also see *Ramaswamy et al.* [2001] for a summary of earlier studies). These studies have clearly illustrated the negative forcing (i.e., cooling) at the TOA due to sulphate, nitrate and organic aerosols and the positive forcing due to black carbon aerosols. One major source of uncertainties in these estimates is a large uncertainty in how the various aerosol species are grouped together (so called mixing state), particularly when the primarily scattering aerosols such as sulfates and nitrates are mixed with absorbing species such as black carbon and when aged aerosols are

0148-0227/05/2005JD006356$09.00

mixed with new particles [*Penner et al.*, 1998; *Haywood and Ramaswamy*, 1998; *Jacobson*, 2001]. Other major sources of uncertainties include: the emission sources for aerosols, particularly black carbon and organics emissions [*Penner et al.*, 1993; *Cooke et al.*, 2002; *Bond et al.*, 2004]; transformation of gases into particles, particularly for organics; wet removal of aerosols; cloud processing of aerosol precursors into fine particles; vertical transport of aerosols across the boundary layer; amongst several others. The purpose of the present study is to estimate the DRF of anthropogenic aerosols globally by adopting an independent method that is less subject to some of the above uncertainties.

[3] Global estimates of DRF have been derived mostly by using an aerosol chemical- transport model (CTM) coupled to a general circulation model (GCM) [e.g., *Takemura et al.*, 2002; *Wang*, 2004]. CTM computes the formation and chemistry of aerosols, and calculates the transport and deposition of aerosols with wind, cloud and precipitation simulated by GCM. The GCM also converts the CTM-simulated aerosol information into the corresponding radiative forcing through the GCM radiation module. A less uncertain approach is to use meteorological fields from reanalyses inferred from radiosonde and satellite observations. Such an example is the Georgia Tech/Goddard Global Ozone Chemistry Aerosol Radiation and Transport (GOCART) model [*Chin et al.*, 2002]. The primary advantage of GOCART is that the analyzed wind fields are closer to reality, when compared with the GCM fields. The GOCART model provides global estimates of aerosol optical depths (AODs), as well as aerosol chemical speciation such as sulfates, organic carbon, black carbon, dust, sea salt and others. *Kinne et al.* [2003] give an excellent review of various recent aerosol simulation studies with a CTM and GCM.

[4] The present study takes an alternate approach which relies heavily on satellite and ground-based observations for the primary aerosol parameters and for additional parameters such as clouds, water vapor, surface albedo and ozone. These parameters are needed for the radiative flux calculations. The primary advantage of our method is that the forcing estimate would not be subject to deficiencies in the GCM or CTM simulations. This approach has been successfully adopted recently for inferring aerosol forcing values from field observations, e.g., the studies of *Ramanathan et al.* [2001] employing data from the Indian Ocean Experiment (INDOEX) campaign, and that of *Huebert et al.* [2003] with the ACE-Asia observations. *Chou et al.* [2002] derived clear sky aerosol forcing over the global ocean from Sea-viewing Wide Field-of-View Sensor (SeaWiFS).

[5] The approach used in this study basically uses the best available global observational results and consists of the following steps:

[6] 1. Use of the Moderate Resolution Imaging Spectroradiometer (MODIS) 2001–2003 satellite data for Aerosol optical depths (AODs). The gaps in satellite data are filled using GOCART [*Chin et al.*, 2002] values. Furthermore, the uncertainties in satellite data are examined using ground-based observations from the AErosol RObotic NETwork (AERONET) [*Holben et al.*, 2001]. The three data sets (MODIS, GOCART and AERONET) are merged using objective statistical assimilation techniques described in section 3.

[7] 2. The primary aerosol parameters such as single scattering albedo, asymmetry parameter and spectral dependence of AODs are obtained from a combination of AERONET and GOCART.

[8] 3. One unique feature of this study is that it uses observed satellite-based three dimensional cloud climatology. This reduces one of the major sources of errors in direct forcing estimates. For example, as shown by *Podgorny and Ramanathan* [2001], the magnitude and even the sign of the aerosol forcing may change depending on cloud amount, cloud albedo and cloud spatial structure. The cloud observations are from the International Satellite Cloud Climatology Project (ISCCP) D2 product [*Rossow and Schiffer*, 1999].

[9] 4. Solar fluxes in the surface-atmosphere system are strongly regulated by surface albedo, water vapor and ozone and we specify these primarily from observations, as described in section 4.

[10] 5. Steps 1 to 4 generate monthly mean values of the global three-dimensional distribution of the relevant atmospheric and surface products, which are inserted into a Monte-Carlo Aerosol Cloud Radiation (MACR) model [*Podgorny et al.*, 2000]. The MACR model was validated extensively [*Satheesh et al.*, 1999; *Podgorny et al.*, 2000] using field data collected during the INDOEX observations [*Ramanathan et al.*, 2001].

[11] We estimated the global (land + ocean) DRF monthly climatology for the period 2001–2003 for anthropogenic aerosols for both clear and cloudy skies. Furthermore, we also conducted detailed sensitivity studies to examine the uncertainties in the estimated forcing values. The data sets are described in section 2, and the techniques of data-model integration are presented in section 3. Section 4 deals with the MACR model description, followed by estimates of forcing in section 5.

2. Data

[12] The various data and their sources are described in this section. Our primary interest is in climatological monthly mean values on a spatial T42 grid of about 2.8° latitude by 2.8° longitude.

2.1. MODIS

[13] The MODIS onboard the Terra satellite gives spectral aerosol measurements globally. The MODIS aerosol algorithm derives the ambient AOD over the oceans [*Tanré et al.*, 2001] and over the continents [*Kaufman et al.*, 1997] on the globe. However, the MODIS data and algorithms are not adequate to retrieve AODs over bright surfaces such as deserts and snow surfaces [*Kaufman et al.*, 1997]. We employed Daily Level 2 AOD products produced at the spatial resolution of a 10-km (at nadir)-pixel array. This product includes global ocean AODs at 550 nm. The land AODs at 550 nm were interpolated from AODs at neighboring wavelengths. We then converted the daily values into monthly means. Any AOD value greater than 1.0 was removed with the assumption that such a large monthly value is most likely a result of cloud contamination. Such large AODs occur over both ocean and land, and occupy a

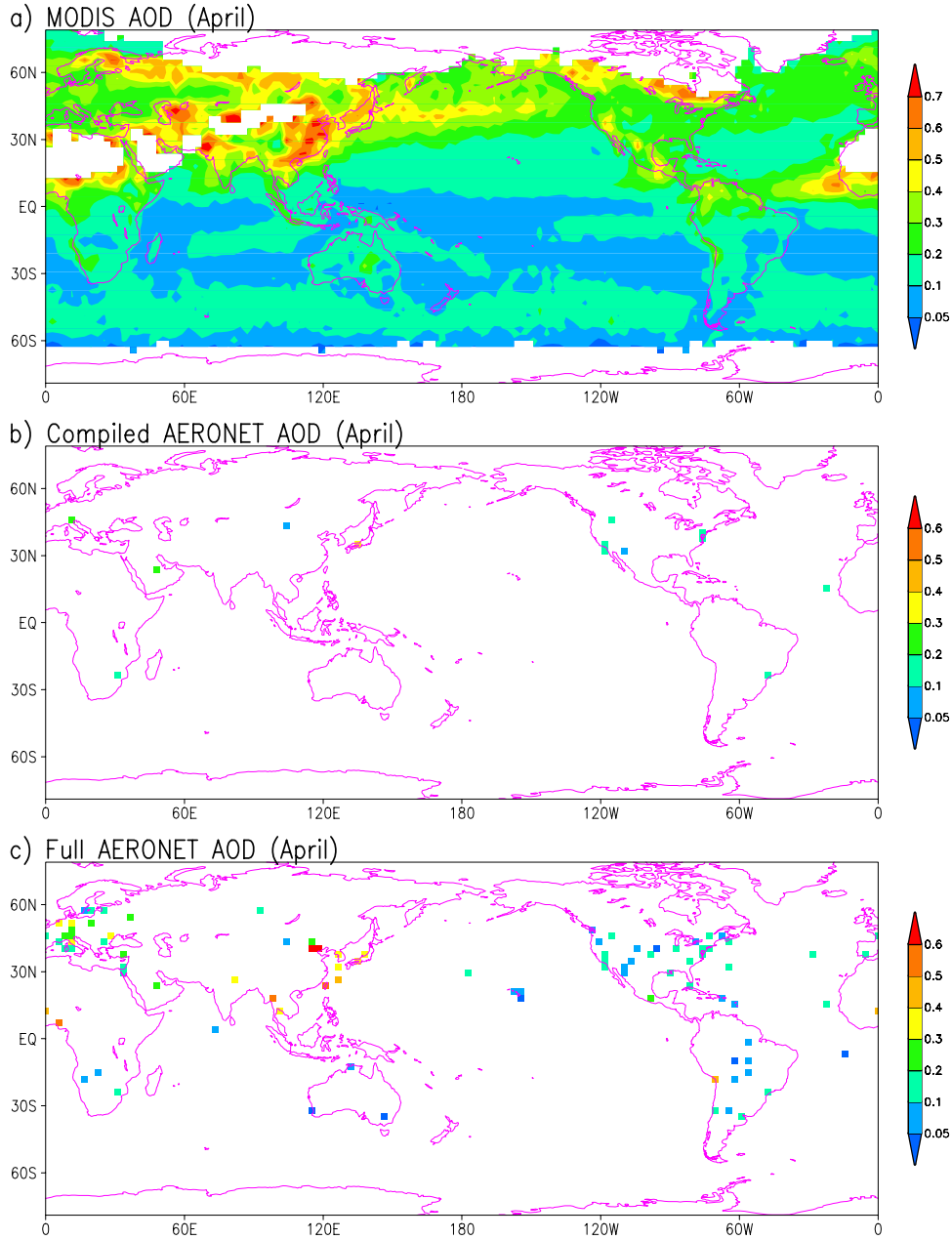

Figure 1. (a) April MODIS AOD averaged for 2001–2003. (b) April AERONET AOD climatology at the sites that have all of April-mean data during 2001–2003. (c) April AERONET AOD climatology at the sites that have any April-mean observation during 2001–2003. In this study, 12 months of AERONET climatology as shown in Figure 1c will be used for the standard estimate of the aerosol forcing. AOD values in all panels are at 550 nm.

very small area (less than 1%). The 10 km × 10 km resolution monthly MODIS AODs were interpolated onto the T42 resolution (approximately 2.8° × 2.8° grid) by averaging the AODs over each T42 grid. These monthly mean AODs for the period 2001–2003 were temporally averaged to produce 12 climatological monthly AODs. Figure 1a displays the processed MODIS AODs for April. As this figure shows, there is a large amount of aerosol loading over Asia during this month. This figure also shows major data gaps over deserts and ice/snow areas due to algorithm limitations over such bright surfaces. As described in section 3, such data void regions were filled by employing the AERONET and GOCART AODs.

2.2. AERONET

[14] AERONET is a worldwide network of automatic Sun- and sky-scanning measurements that are monitored and maintained by the NASA Goddard Space Flight Center [*Holben et al.*, 2001]. Data have been generated since 1993. At each AERONET site, 50 attenuation and 10 sky-radiance measurements are taken during a day [*Kinne et al.*, 2003]. The AERONET team processes these measurements to

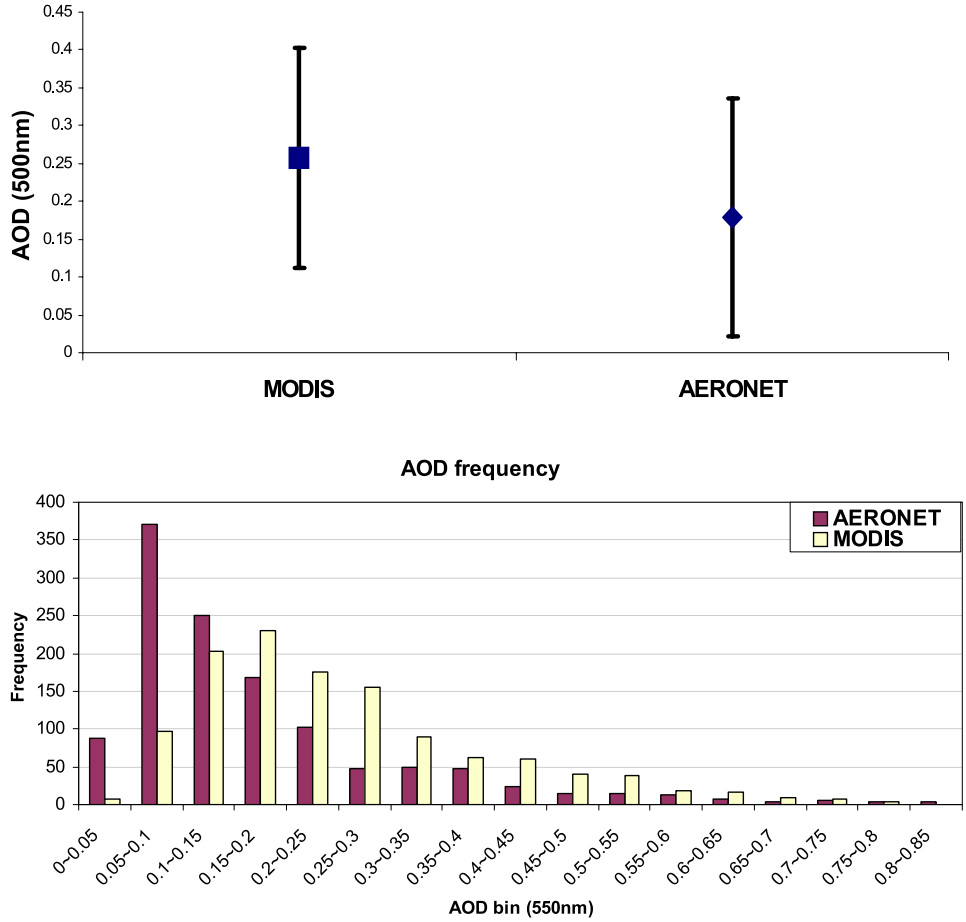

Figure 2. Comparison of monthly AERONET AODs and monthly MODIS AODs collocated in time and space (2001–2003). Any AOD greater than 1.0 was removed. Upper panel shows mean and ±1 × S.D. The mean AERONET AOD is 0.179, and the mean MODIS AOD is 0.256. The difference is 0.077. The r.m.s. of (MODIS – AERONET AOD) is 0.145. The global area mean of (MODIS – AERONET AOD) is 0.044 (see Table 1). Lower panel shows that most of AERONET AODs are less than 0.2 while MODIS AODs often show very high values. Figure 1c shows the AERONET-MODIS collocated locations for April.

derive the optical parameters needed for our study, which are: AOD, single scattering albedo (SSA) and asymmetry parameter. We employed the level 2 product, i.e., the quality assured product for cloud screening, and calibration. The AERONET team estimates AOD, SSA and asymmetry parameter at 440 nm and 670 nm and we interpolated these wavelength values to obtain values at 550 nm. The interpolation was linear for SSA and asymmetry parameter and by natural log function for AOD.

[15] We treated AODs as providing the ground truth for validating and for estimating the uncertainty in the satellite derived aerosol observations. Instantaneous (as opposed to time averaged) MODIS AODs have been compared with time- and space-collocated AERONET AODs by several studies [*Chu et al.*, 2002; *Remer et al.*, 2002; *Hao et al.*, 2002]. *Chu et al.* [2002] compared the MODIS AOD and AERONET AOD over the ocean, *Remer et al.* [2002] compared the two over land, and *Hao et al.* [2002] over Africa. In all these comparisons, a linear regression fit was sought in the form of "MODIS AOD = slope * AERONET AOD + interception". Overall, the slope is slightly less than 1.0 and the intercept is slightly greater than 0.0. In summary the instantaneous MODIS values seem to agree well with the instantaneous AERONET AODs. Since we are interested in monthly mean values, we undertook a comparison of the monthly mean AODs between MODIS and AERONET collocated in time and space (Figure 2) and found much larger differences between the two. In addition to the large differences shown in Figure 2, we find that monthly AERONET AODs are not always linearly correlated with monthly MODIS AODs. When AOD is large (>0.3), AERONET AOD tends to be larger than MODIS AOD. One possible explanation for this trend is that the assumed SSA may be higher than the actual SSA, resulting in an underestimation of the retrieved AOD by MODIS. When AOD is small (<0.2), AERONET AOD is generally smaller than MODIS AOD. The statistics of the frequency distribution of the AODs by the two data sets yield some insights into the causes of the differences. Most of the monthly mean AERONET AODs are less than 0.2 whereas more than half of the MODIS AODs are greater than 0.2. Furthermore, AERONET samples a significantly larger number days of

very low AODs (<0.1) than MODIS. Since the instantaneous values are in much better agreement, the differences between the two data sets are most likely due to differences in sampling the clear, the cloudy and the overcast skies. MODIS samples a scene about once a day while AERONET samples it every 15 minutes. Thus the contamination of the scene by clouds would be much larger in MODIS. Cloud contamination would almost always enhance the retrieved optical depth; a 5% cloud contamination by a cloud of optical depth (with typical values of 5 to 20) is sufficient to bias AOD by about 0.05 to 0.1. This would also help explain why the frequency of very small (<0.1) monthly mean AODs are much lower in MODIS. In summary, we can not reliably claim that monthly AERONET values are more reliable and hence we bracket the uncertainty in the forcing by estimating it with just MODIS and compare it with MODIS and AERONET combined.

[16] Monthly AERONET AODs were averaged from 2001 to 2003 for each calendar month and also for each T42 grid box. Figure 1b shows climatological AERONET AODs in April over the sites that have all 3 monthly AODs during the 2001–2003 period. We generated another AERONET estimate by taking any site that has at least one monthly AOD (Figure 1c). Many of the sites shown in Figure 1c have only one monthly value during the whole 3-year period in April, and so the values in this climatology may not accurately represent the true 3-year average. However we use this AERONET AOD estimate for this study, because the advantage of having more sites outweighs the disadvantage. Climatological AERONET SSAs and asymmetry parameters were processed in the same way except that the temporal averages were weighed by the corresponding AODs. In order to examine the sensitivity to interannual variations in AODs, we also generate climatological AODs, SSAs and asymmetry parameters with 1993–2003 averaged AERONET products. In section 5, we examine the uncertainty in our forcing estimates due to the differences in all these data sets.

2.3. GOCART

[17] The GOCART (GeorgiaTech-Goddard Global Ozone Chemistry Aerosol Radiation and Transport) model simulates black carbon (BC), organic carbon (OC), sulfate, sea salt and dust AODs at 550 nm separately [*Chin et al.*, 2002]. *Chin et al.* [2002] give a summary of the GOCART model system. GOCART adopts published emission inventories and assimilated (observed) meteorological fields as input to the CTM, which in turn computes aerosol variables. The total AOD and its BC fraction over India and the northern Indian Ocean compare to the INDOEX observations [see *Ramanathan et al.*, 2001] favorably. For example, in both the GOCART simulation and INDOEX observation, the total anthropogenic AOD in S. Asia from January to March is about 0.2∼0.4 and the corresponding BC fraction is about 20%.

[18] The GOCART model produces a global gridded output at the 2.5° × 2.0° resolution and the results are archived on a monthly scale from January 2000 to July 2002. The GOCART model simulation includes the anthropogenic sulfate/OC AODs and the fine-mode dust/sea salt AODs for September 2000, March 2001 and April 2001. All these products were interpolated onto the T42 resolution. BC, OC, sulfate, dust and sea salt AODs were temporally averaged from January 2000 to July 2002, giving the monthly climatology.

2.4. ISCCP

[19] The ISCCP (International Satellite Cloud Climatology Project) was established at NASA Goddard Institute for Space Studies in 1982 and the project second phase began in 1995 [*Rossow et al.*, 1996]. The ISCCP integrates various satellite measurements and produces global cloud data. We downloaded the D2 product, which is the monthly mean of the D1 data. The D2 data set has 130 variables. Out of these, we extracted cloud amount and cloud visible optical depths of all the clouds. The D2 product has 6 low-cloud types, 6 mid-cloud types, and 3 high-cloud types. We combined these 15 types of water and ice low-level (cumulus, stratocumulus, stratus), middle-level (altocumulus, altostratus, nimbostratus) and high-level (cirrus, cirrostratus, deep convective) cloud into 4 types: low, mid, high and deep convective clouds. In combining the cloud amounts, no overlap was assumed between clouds in each of 4 types. The cloud optical depths were averaged by weighting the optical depth with the individual cloud fraction and normalizing with the total cloud cover under each of the four cloud types adopted in this study.

[20] The D2 product is stored on an equal area grid and we interpolated the values onto the T42 grid. After this, temporal means were taken for the period from January 1999 to September 2001, giving 12 months of cloud climatology. Figure 3 shows the April cloud climatology. In addition, we created another cloud climatology by employing a temporal mean for the period from January 1990 to September 2001. In section 5, we examine the uncertainty in our forcing estimates due to interannual and decadal variability, by adopting the two cloud climatology data sets in the radiative flux calculations.

3. Data Integration

[21] MODIS, AERONET and GOCART climatology products were assimilated statistically. The scheme was developed under the assumption that AERONET data are more accurate than MODIS data and MODIS data, in turn, are more accurate than GOCART model results. We obtained the anthropogenic fraction of the aerosol forcing by subtracting the natural aerosol forcing from the total (anthropogenic + natural) forcing. The natural aerosol fraction was estimated from two independent sources. The first source is the GOCART model output for the natural component of AOD. For the second source, we employ the ratio of the MODIS_AOD_Large (i.e., AOD due to larger aerosol particles) to the total MODIS_AOD as an index for the fraction of natural aerosols, since anthropogenic aerosols are mostly sub-micron size particles. This technique works only over the oceans, since MODIS_AOD_Large is available only for oceanic regions. Below, we explain the techniques in more detail.

3.1. Aerosol Optical Depth (AOD)

[22] The assimilation process takes place in two steps: First, we fill the gaps in MODIS_AODs (Figure 1a) with GOCART_AODs using the iterative difference-successive

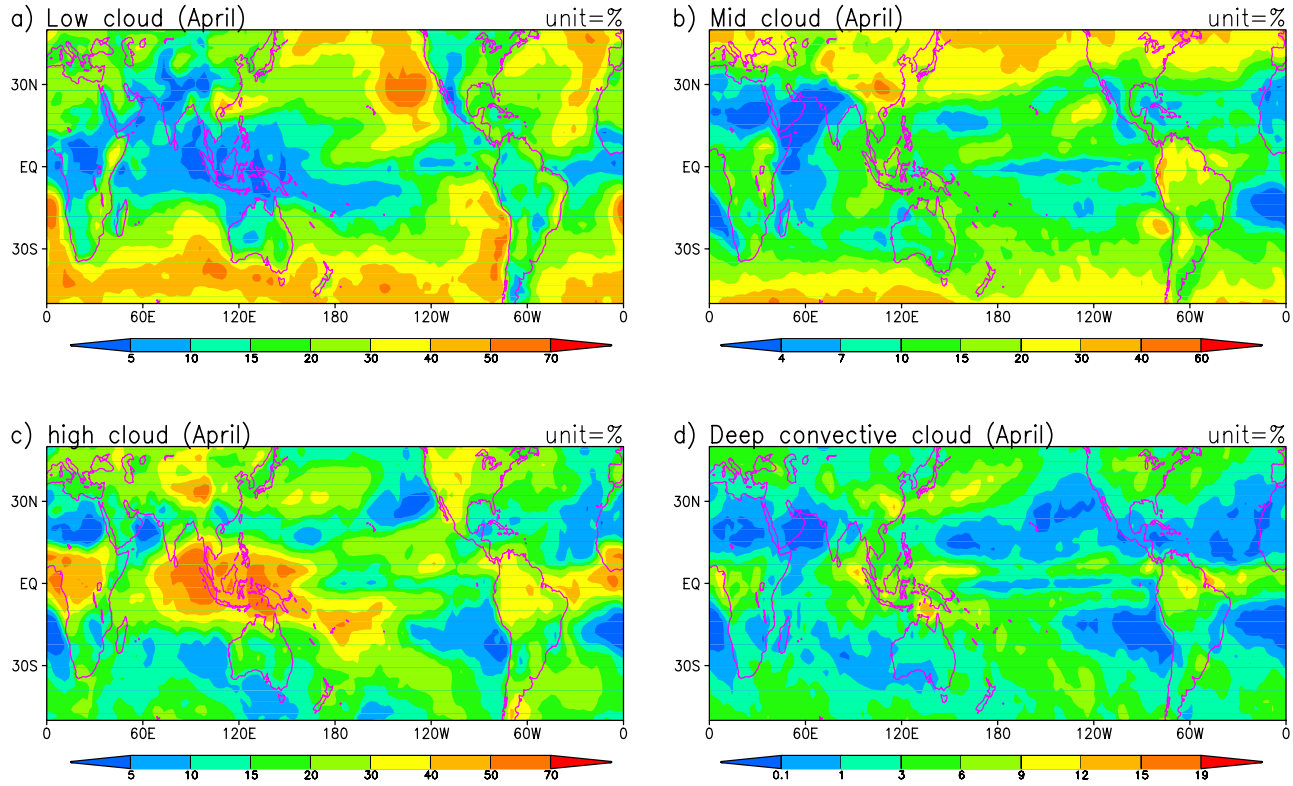

Figure 3. Cloud fraction climatology for the period January 1999 to September 2001. The data were obtained by processing the ISCCP D2 product.

correction method designed by *Cressman* [1959]. The resulting MODIS+GOCART_AODs constitute one estimate for the global distribution of gridded monthly-mean AODs. The second step, which produces another estimate for the global AODs, employs an iterative correction scheme to relax the MODIS+GOCART_AODs to values that are consistent with and closer to the AERONET_AODs.

[23] Filling gaps in MODIS with GOCART: *Cressman* [1959] originally developed his technique to transform irregularly located stations' observations to a gridded data set. The implicit assumption we made is that the MODIS_AODs are more reliable than GOCART AODs. At grid points where there are no MODIS-AODs, we employ the GOCART values after correcting for its errors, where the error of a GOCART-AOD is estimated from a neighboring grid point which has both MODIS_AOD and GOCART_AOD. We implemented the Cressman technique as follows: (1) start with the GOCART_AODs (which have no gaps); (2) at each T42 grid point where there is an available MODIS_AOD, calculate the ratio with respect to the corresponding GOCART_AOD; (3) use this ratio to correct the GOCART_AODs over the neighboring grid points where there are no MODIS values; and (4) repeat steps 2–3 to all the other grids that have MODIS_AODs. The whole procedure is iteratively repeated, starting from neighboring grids 3 grid-distance away from each MODIS_AOD point in the first iteration, reducing the distance by one grid at each iteration. We refer to *Cressman* [1959] for other details. Figure 4a shows the MODIS+GOCART AODs. Compared to Figure 1a, we see no conspicuous discontinuity along the border of regions with gaps in MODIS_AOD.

[24] Assimilating AERONET_AODs: The *Cressman* [1959] approach does not work well for spatially inhomogeneous and sparse distributions of observing stations such as AERONET sites. We developed a technique that respects the spatial pattern of the MODIS+GOCART_AODs and fully uses the AERONET_AODs. *Reynolds* [1988] faced a similar issue when he attempted to combine in situ SST observations and satellite-derived SSTs. Reynold's technique involves solution of a Poisson equation, which forces the final product to adopt the spatial pattern of satellite observations and import the in-situ SSTs. We found that the direct application of his technique was unsuitable for the AERONET station distributions.

[25] We employed the following technique for assimilating the AERONET_AODs into MODIS+GOCART_AODs. At each T42 grid, say j, with a MODIS + GOCART_AOD (denoted by MG_AODj in equation (1)), we let:

$$\mathrm{MGA\_AODj} = MG\_AODj \times \frac{\sum_i \frac{AERONETj,i}{dj,i^4}}{\sum_i \frac{MG\_AODj,i}{dj,i^4}} \qquad (1)$$

where MGA_AODj is the adjusted new value of the AOD at grid j, *AERONETj,i* is an AERONET_ AOD at station location i nearby the grid j, dj,i is the distance between j and i, *MG_AODj,i* is the MODIS + GOCART_AOD at the grid which has the AERONET_AOD location i. It is possible and likely that at any grid j, there are quite a few AERONET AODs nearby, and if this is the case the algorithm weights them according to the distance from the

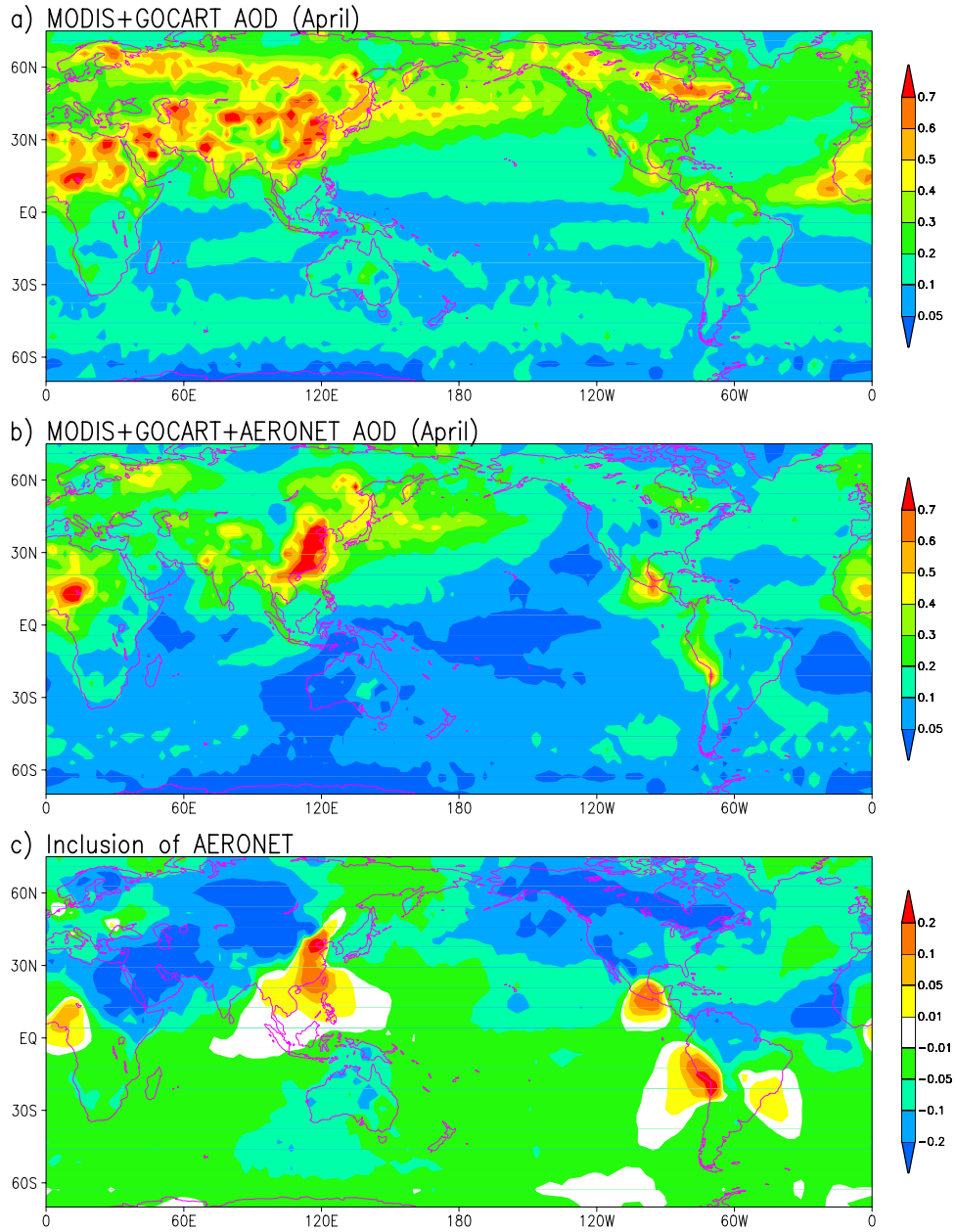

Figure 4. (a) 550 nm AOD by integrating the MODIS AOD and GOCART AOD. (b) 550 nm AOD by integrating AERONET AOD and MODIS+GOCART AOD. (c) AOD climatology in April.

location of the grid j as in equation (1). The algorithm searches for all the AERONET AODs semi-globally. However, because of the weighting with the fourth power of the distance, the AERONET locations closest to the grid are weighted the most.

[26] Figure 4b displays the MODIS + GOCART_AODs adjusted using the AERONET_AODs as just described. Figure 4c, which shows the difference between the MODIS +GOCART+AERONET_AODs and MODIS+ GOCART_AODs, reveals the impact of the AERONET AODs. As Figure 4c shows, the inclusion of AORONET AODs decreases the estimated AODs in most parts of the globe, especially in North America, and southwest and central Asia. Including AERONET products also reduces the AODs across the northern Pacific and the equatorial Atlantic. The MODIS+GOCART+AERONET_AOD as shown in Figure 4b is considered our standard AOD climatology estimate for the aerosol forcing computation. In Figure 4b, the coastal area of China has the largest aerosol loading around the world in April. The annual-mean AOD (not shown) is still largest in this area, reaching values close to 0.9. Africa and India also have large values of AODs.

[27] Fraction of natural AODs from GOCART: We use two independent sources for estimating the natural fraction of the total AODs. The first source is the GOCART model which is used as the standard estimate. The GOCART model gives individual AODs for BC (black carbon), OC (organic carbon), sulfate, sea salt and dust. In this study, dust and sea salt are assumed to be 100% natural and BC is assumed to be

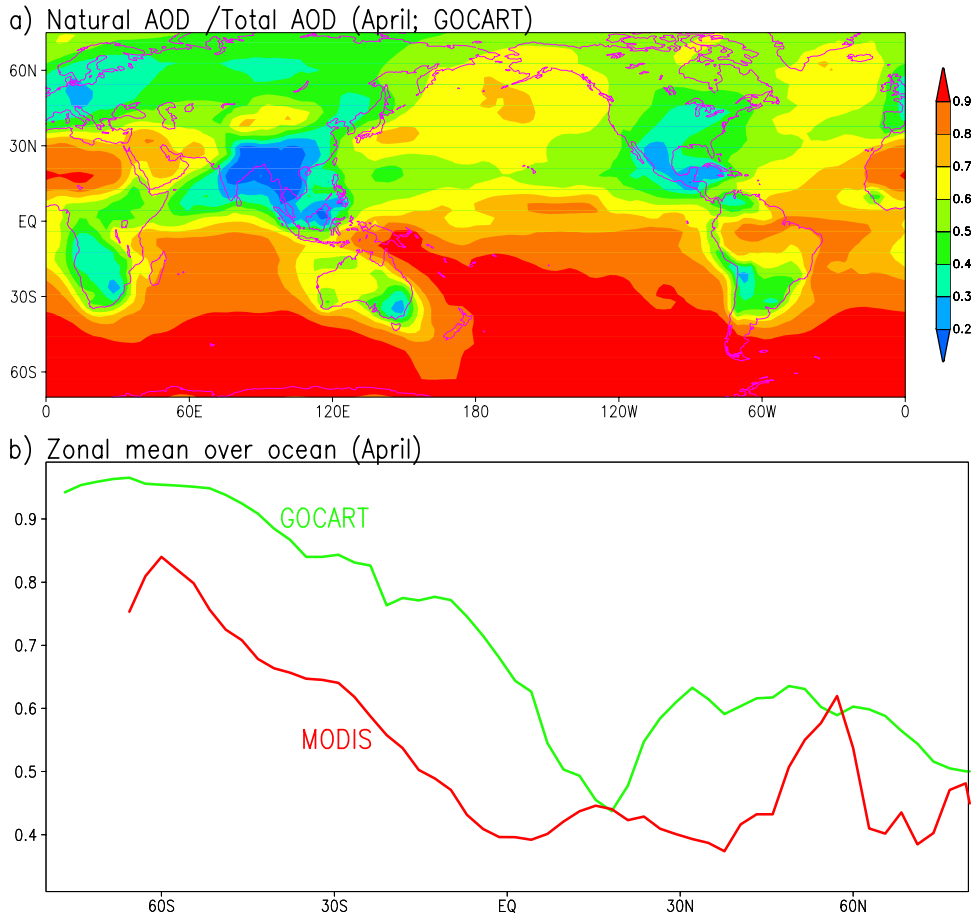

Figure 5. (a) Ratio of natural aerosol optical depth to total AOD, as computed from the GOCART product. (b) Ratio of zonal-mean natural AOD to zonal-mean total AOD with the GOCART.

100% anthropogenic. The GOCART model simulation also includes the natural fraction of sulfate and OC AODs for September 2000, March 2001 and April 2001. We calculated the natural ratio of sulfate and OC for these 3 months, and multiplied these ratios with the annual cycle of sulfate and OC to derive the annual cycle of natural sulfate and OC. The ratios from September were used from July to December, those from March used from January to March, and those from April used from April to June. Then, for each calendar month, we computed the ratio of the natural AOD to the total AOD in the GOCART simulation. This ratio, referred to as the "natural" ratio, is used in combination with the integrated total AOD (Figure 4b) to obtain the natural and anthropogenic AODs. Figure 5a shows the global distribution of the natural ratio in April. As is clear from this figure, low natural ratios span South Asia, Southeast Asia, China and Mexico. Most of the southern hemisphere has high natural ratios. For land regions, northern Africa has the largest amount of natural aerosol due to the dominance of the Saharan dust, while anthropogenic aerosols dominate the coastal area of China. Annual mean natural (or anthropogenic) AOD pattern (not shown) also points to northern Africa as the strongest natural aerosol region and the coastal China as the strongest anthropogenic aerosol region. Other regions with significant annual-mean anthropogenic aerosol loadings are Mexico, South and Southeast Asia, the west coastal South American region and northeastern Russia.

[28] Global mean of AOD is 0.13 for total (anthropogenic + natural) aerosols, and it is 0.05 for anthropogenic aerosols (see Table 1). Thus, in our estimate, the anthropogenic fraction of the global aerosol optical depth is about 40% of the total AOD. However, anthropogenic aerosols have lower SSAs, and their influence on the surface solar radiation or atmospheric absorption is greater than that of natural aerosols.

[29] Fraction of natural AODs from MODIS: In order to understand the potential uncertainty in the GOCART natural fraction, we assume that the MODIS_AOD for large mode particles (effective diameter >1 μm) is a measure of natural aerosols. The MODIS retrieval of large particle AOD is

Table 1. Area Mean of AOD/SSA Used in This Study for the Standard Estimate of the Aerosol Forcing[a]

	Global	NH	SH	Land	Ocean
Total (Natural + Anthropogenic) Aerosol					
AOD (550nm)	0.127	0.160	0.094	0.183	0.104
SSA (550nm)	0.942	0.939	0.947	0.928	0.952
Anthropogenic Aerosol					
AOD (550nm)	0.051	0.070	0.032	0.095	0.033
SSA (550nm)	0.868	0.876	0.848	0.874	0.860

[a]AERONET observations were included for AOD/SSA values in this table. GOCART products were used to derive the anthropogenic fraction. Global mean of the total AOD without AERONET observations is 0.171.

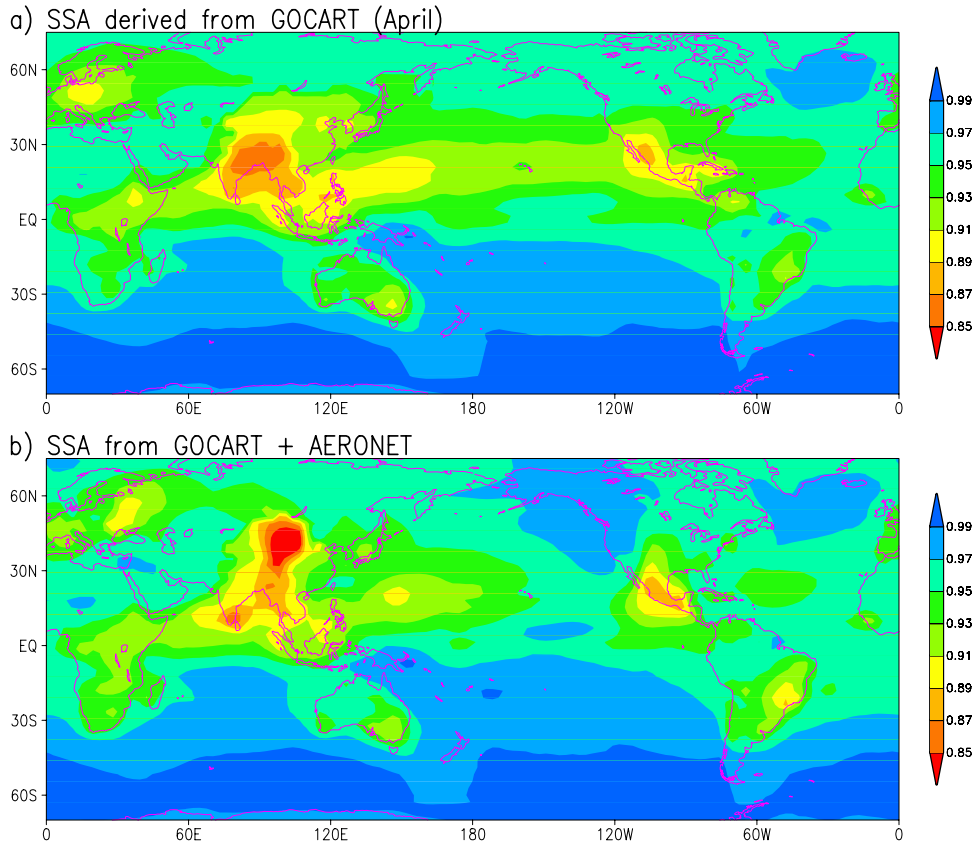

Figure 6. (a) April SSAs derived from the GOCART product. (b) SSAs nudged towards AERONET SSAs. SSA values in all panels are at 550 nm.

restricted to oceanic regions, and in Figure 5b we compare the natural AOD fraction from MODIS with GOCART values. The latitudinal variations are similar between the two data sources, but our estimate of the natural fraction from MODIS is systematically smaller than GOCART simulations by about 0.1 to 0.2. This is expected since dust and sea salt also contain small size particles and our assumption that natural aerosol contains only large mode should underestimate the natural loading of aerosols. Thus the MODIS derived natural fraction should provide a lower (upper) bound on the natural (anthropogenic) fraction.

3.2. Single Scattering Albedo (SSA)

[30] The first guess for the global SSAs at 550 nm was obtained from the GOCART simulations which are subsequently adjusted with the AERONET SSAs. GOCART_SSAs were derived by weighting the individual SSAs for BC, sulfate, OC, dust and sea salt with their respective AODs. The SSA for each of the five aerosol types is assigned as follows. Sulfate, OC and sea salt are assumed to have a SSA of 1.0 (i.e., conservative scatterers) and the BC SSA is assigned a value of 0.2 [*Satheesh et al.*, 1999]. The dust SSA is allowed to vary from 0.9 to 0.98 depending on the amount of BC. When the ratio of BC_AOD to BC+dust_AOD is less than 0.1, the dust SSA is 0.98, and when the ratio is greater than 0.5, the dust_SSA is set to 0.90. For ratios between 0.1 and 0.5 ratios, the dust SSA linearly decreases from 0.98 to 0.9. Over China and the northern Pacific, the dust SSA is prescribed differently. The dust_SSA for all of China is assumed to be 0.9 and it linearly increases from 0.9 over the north-western Pacific (off of China) to about 0.95 over the north-eastern Pacific (off of the west coast of N. America). The parameterization described above for dust SSA was motivated by the AERONET results reported in *Eck et al.* [2001, 2005] and the field studies off of Asia reported in *Clarke et al.* [2004] and *Kim et al.* [2005].

[31] Figure 6a displays the SSAs that were derived from the GOCART simulations as described above. These SSAs were subsequently adjusted with the AERONET SSAs. The adjustment procedure is similar to that described in the earlier sub-section for AOD. The corrected SSAs, as used in this study, are shown in Figure 6b. In both panels of Figure 6, South Asia, Southeast Asia and Mexico stand out as regions of highly absorbing aerosols. One of the interesting differences between GOCART_SSAs (Figure 6a) and GOCART+AERONET_SSAs (Figure 6b) is that the eastward increase over the northern Pacific is greater when we use AERONET.

[32] The natural aerosol SSAs are derived, by taking dust, sea salt and natural sulfate/OC particle optical depths simulated by the GOCART. The SSA for natural dust is set to 0.98 and is set to 1 for all other natural species.

3.3. Asymmetry Parameter (g)

[33] Global asymmetry parameters are derived similarly to SSAs, by estimating them with the GOCART AODs and

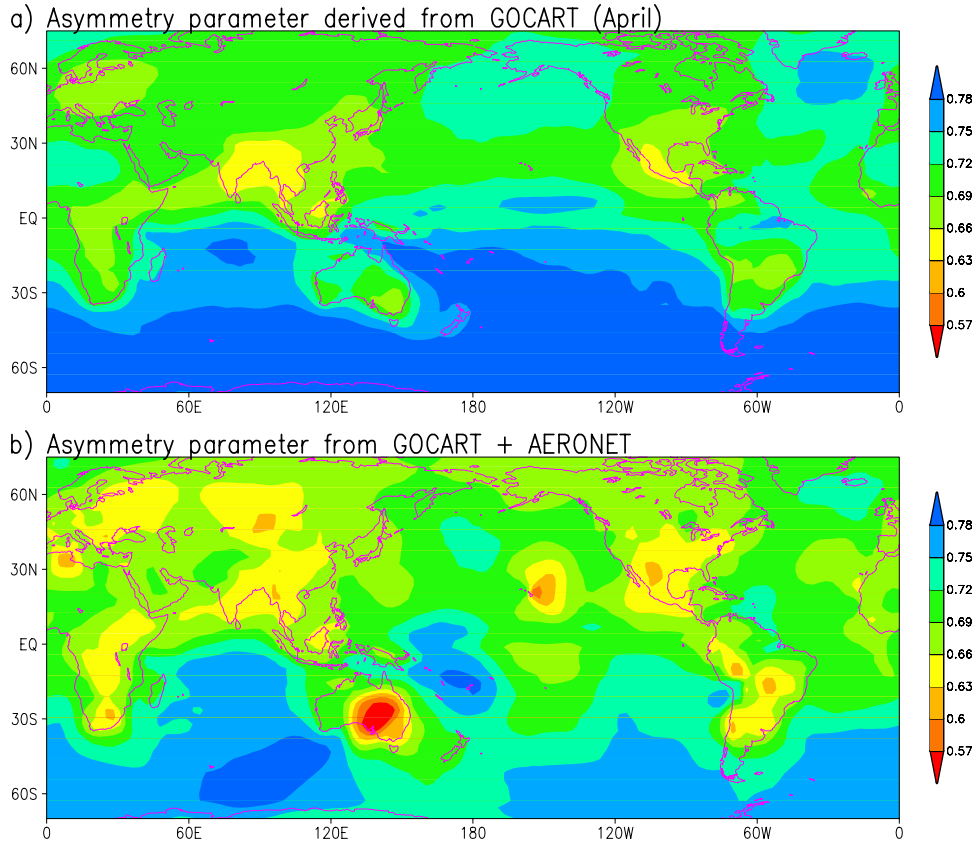

Figure 7. (a) April asymmetry parameters derived from the GOCART product. (b) Asymmetry parameters nudged towards AERONET asymmetry parameters. Asymmetry parameter values in all panels are at 550 nm.

then adjusting them with the AERONET product. We adopt the Optical Properties of Aerosols and Clouds (OPAC) data [*Hess et al.*, 1998] to assign the asymmetry parameters of BC, sulfate, OC, dust and sea salt particles. The OPAC provides different asymmetry parameters for different sizes of dust and sea salt aerosols, and the GOCART simulation also distinguishes small dust from large dust and fine sea salt from coarse sea salt aerosol. The BC, OC, sulfate, sea salt and dust asymmetry parameters are weighted with the corresponding GOCART_AODs.

[34] Figure 7a shows the asymmetry parameter (g) as derived with the GOCART AODs, and Figure 7b displays the asymmetry parameter after it was adjusted with AERONET observations. This adjustment procedure was similar to the one described for AODs., except that the difference between the AERONT and GOCART estimates, rather than their ratio, is used to correct the GOCART-derived asymmetry parameters. The asymmetry parameters of natural aerosols are directly adopted from the OPAC data.

3.4. Spectral Dependence

[35] The global AOD, SSA and asymmetry parameters described thus far were all estimated at 550 nm wavelength. The wavelength dependences of all of the three parameters were obtained from the so-called Angstrom coefficient (α), where α satisfies the following equation [see *Eck et al.*, 2001]:

$$X(\lambda) = X(550\,\mathrm{nm})\left(\frac{\lambda}{550}\right)^{-\alpha} \tag{2}$$

where X can be AOD, SSA or g (the asymmetry parameter). We adopted the following parameterizations for α such that the spectral dependencies adopted by us are consistent with the AERONET results published in the literature [e.g., *Dubovik et al.*, 2002; *Eck et al.*, 2001].

$$\alpha(AOD) = \frac{1.9 \times AOD\_BC + 1.7 \times AOD\_(OC + sulfate) + 1.4 \times AOD\_seasalt + 0.6 \times AOD\_dust}{total\_AOD} \tag{3}$$

$$\alpha(SSA) = \frac{0.078 \times AOD\_BC + 0.0 \times AOD\_(OC + sulfate) + 0.012 \times AOD\_seasalt - 0.068 \times AOD\_dust}{total\_AOD} \tag{4}$$

$$\alpha(g) = 0.1288 \times \alpha(AOD)^3 - 0.1983 \times \alpha(AOD)^2 + 0.0618 \times \alpha(AOD) + 0.0502. \quad (5)$$

4. Radiative Transfer Model

[36] We adopted the Monte-Carlo Aerosol Cloud Radiation (MACR) model described in *Podgorny et al.* [2000] to compute the aerosol radiative forcing. The MACR model was developed and validated extensively during INDOEX [*Satheesh et al.*, 1999; *Podgorny et al.*, 2000; *Podgorny and Ramanathan*, 2001; *Ramanathan et al.*, 2001]. The model was deployed on the T42 grid (approximately 2.8° × 2.8° resolution). In spite of the fact that the model three dimensional inputs were created only on a monthly mean basis, the MACR model was run for all 365 days of the year to account accurately for the variations in the solar zenith angle, declination and eccentricity of the orbit of the planet around the sun. For each day, the monthly inputs were interpolated in time. The model output was averaged for each calendar month. In what follows, we will describe specific improvements to MACR that were made to adopt MACR for this study.

4.1. Conceptual Description of the Model Frame

[37] While previous realizations of MACR were based on explicit photon tracing in three-dimensional cloud fields, the updated MACR model for this study was built upon the so-called Monte Carlo Independent Column Approximation (McICA) approach [*Pincus et al.*, 2003]. The key element of this new version of MACR is the Monte Carlo radiative transfer solver combined with the Monte Carlo integration in the multi-dimensional parameter space that includes solar zenith angles, aerosol-cloud configurations and spectral bands. We deployed 40,000 photons for each day. The advantage of the Monte Carlo approach for solving the radiative transfer equation is that it provides the atmospheric flux values far more accurately than those obtained with two-stream approximations [e.g., *Barker et al.*, 2003] for both clear and cloudy skies.

4.2. Cloud Effects

[38] As discussed briefly in introduction, clouds significantly influence the direct radiative effects of the aerosol at the TOA, in the atmosphere and at the surface. For example, it has been shown [*Podgorny and Ramanathan*, 2001, and references therein] that the sign of the direct aerosol forcing at TOA depends critically on the fraction of low clouds. It is therefore essential to quantify the effects of clouds on the aerosol forcing on both global and regional scales. What distinguishes our study from most other studies of the aerosol forcing estimates is the usage of observed cloud data. The ISCCP data are the only global three dimensional source for clouds in this study. As described in section 2.4, the various ISCCP-derived clouds were processed into 4 types: low, mid, high and deep-convective clouds. Cloud overlap treatment between low, mid and high clouds follows the overlap scheme described in *Chen et al.* [2000]. Deep convective clouds are explicitly taken into account.

[39] Cloud optical thickness and fraction for selected cloud types are the two most important cloud parameters with respect to the all-sky aerosol radiative forcing [*Podgorny and Ramanathan*, 2001]. Cloud SSA (assuming that no aerosol particle is trapped in cloud drops) is nearly 1 in the visible region of the spectrum and it decreases slightly in the near infrared. Cloud SSA and asymmetry parameter have been computed following the National Center for Atmospheric Research (NCAR) Community Atmospheric Model (CAM) algorithm. We use external mixing approximation for the interstitial aerosol due to the lack of information on the mixing properties of absorbing aerosols and cloud drops.

4.3. Surface Albedo and Other MACR Input Parameters

[40] The land surface albedo was obtained from the ECMWF surface solar radiation reanalyses (1998–2001 mean). The ECMWF reanalysis project incorporated various observations (including satellite observations) into a GCM to produce consistent and continual outputs [*Simmons and Gibson*, 2000]. The ocean surface albedo that has been adopted for this study is a hybrid of the ocean albedo scheme given in *Briegleb et al.* [1986] and the clear-sky visible surface albedo data of ISCCP. First, we start with the ocean surface albedo parameterization of *Briegleb et al.* [1986] which, in turn, was derived from the observational study by *Payne* [1972], who measured the ocean surface albedo off the U.S. east coast. The Briegleb et al.'s scheme yields the surface albedo as a function of solar zenith angle and thus local time.

[41] The ISCCP data reveal variations in the ocean surface albedo in space and time that are larger than what we would estimate from the *Briegleb et al.*'s [1986] albedo scheme. In order to account for this spatial and temporal variation of ocean surface albedo, we scale the Briegleb et al.'s ocean surface albedo (estimated as a function of local time) with the ISCCP_albedo (lat × lon), and then apply a scaling factor (a scalar number) such that the adjusted ocean surface albedo for the U.S. east coast is equal to the Briegleb et al.'s formula. This scaling factor is equal to (daily-averaged Briegleb et al.'s albedo)/(ISCCP_albedo at the east coast of USA). The albedo over sea ice surfaces (i.e., grids that contain some ice) was set to 70% of the visible ISCCP albedo, because the visible albedo over sea ice is larger than the wavelength-integrated (from 0.3 to 4 μm) albedo by about 30%.

[42] As for the model atmosphere, gaseous absorption is implemented using correlated k-distribution approach [*Vogelmann et al.*, 2001]. The model uses 25 bands and a total of 3132 pseudo-monochromatic calculations to cover the solar spectrum from 0.25 to 5.0 μm (see *Vogelmann et al.* [2001] for more details). The model atmosphere includes a standard profile of ozone and a standard profile of precipitable water. The vertically-integrated amount of ozone was derived from the Tiros Operational Vertical Sounder (TOVS) and it was averaged from January 1990 to September 2000 for the model input; ISCCP D2 product includes this ozone data. The vertically-integrated precipitable water was derived from the TOVS onboard NOAA-12 satellite and it was averaged from 1992 to 1997 (from NASA/GSFC). Both ozone and precipitable water inputs are a function of time and location. The surface orography effects are taken into consideration by removing air and any cloud below elevated surface.

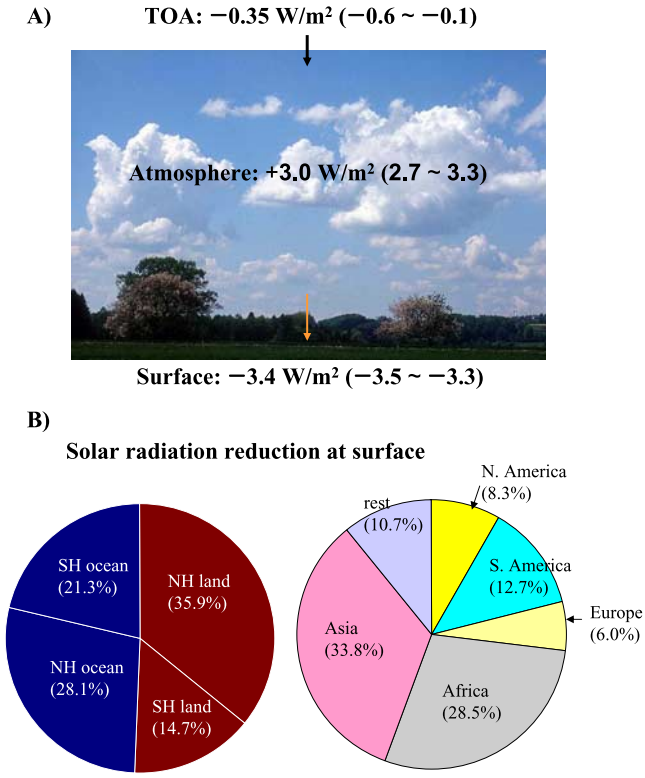

Figure 8. Annual and global mean anthropogenic aerosol forcing. (a) Our best estimate and its uncertainties are presented. (b) We partition the surface forcing estimate by region. The direct aerosol effects on solar radiation are shown in this figure (and all the subsequent figures).

[43] The aerosol profile is assumed to be uniform from the surface to 3.4 km in the tropics (30°S–30°N) and uniform to 2 km in the extratropics. Above this height, the aerosol density is decreased exponentially.

5. Aerosol Forcing Estimates

[44] The MACR model was run with the features discussed in the previous sections. The MACR estimates with the MODIS, GOCART, 2001–03 AERONET and 1999–2001 ISCCP data are referred to as the standard estimates. For global-annual mean conditions, the incoming solar radiation at the TOA is 341.8 W/m^2 and the outgoing reflected solar radiation at the TOA is 98.9 W/m^2, yielding a value of 29% for the TOA albedo, which agrees with measured values from the Earth Radiation Budget Experiment (ERBE) satellite data [*Harrison et al.*, 1990; *Ramanathan et al.*, 1989] for the 1985 to 1989 period. For a further validation, the model was run without clouds and compared to the ERBE clear sky data. The ERBE produced a data set of global clear-sky outgoing solar radiation at the TOA from 1985 to 1989. The global mean ERBE value is 54.1 W/m^2 and the MACR estimated clear sky outgoing solar flux is 52.2 W/m^2. For the 60°S–60°N, the ERBE value is 49.7 W/m^2 while the MACR estimate is 48.6 W/m^2. For the anthropogenic aerosol forcing, we compared the MACR estimates for the January–March averaged surface forcing for the northern Indian Ocean with the observed estimate during the INDOEX (Indian Ocean Experiment [*Ramanathan et al.*, 2001]), and the two estimates agreed with each other within 25%; the agreement might improve if comparison is made with multi-year observations.

[45] The summary of the solar forcing results from the standard version of MACR is shown in Figure 8 and a summary of the average aerosol parameters are given in Table 1. Referring first to Table 1, global-mean anthropogenic AOD (0.05) is as much as 40% of the total global mean AOD (0.13). The northern hemisphere has more than twice as much anthropogenic AOD as the southern hemisphere (0.07 for NH compared with 0.03 for SH). Furthermore, the global mean land averaged anthropogenic AOD (0.095) is larger by about three times than the ocean averaged value (0.033). The SSA for the anthropogenic aerosols ranges from 0.85 to 0.88, while when it is combined with natural aerosols the aerosols become less absorbing and the SSA increases to 0.93 to 0.95 (Table 1).

[46] The results for the forcing shown in Figure 8 are for average cloudy skies, alternately referred to as all-sky conditions. The global mean forcing value is −0.35 Wm^{-2} at the TOA, +3.0 Wm^{-2} in the atmosphere and −3.4 Wm^{-2} at the surface. Thus as has been noted earlier [*Ramanathan et al.*, 2001], when we include aerosol absorption, the TOA forcing is a small difference between the large negative forcing at the surface and the large positive forcing of the atmosphere. For the results shown in Figure 8, the TOA forcing is just 10% of the surface forcing. We estimated the uncertainty in these estimates by redoing MACR calculations with various versions of the input data sets (see Table 2) and the resulting values are shown as ranges in Figure 8a.

[47] The uncertainty in our global-annual mean anthropogenic forcing estimate was explored by conducting several sensitivity studies with MACR. We changed the MACR model input parameters in the directions that reflect our lack of confidence in aerosol data. As Table 2 summarizes, the first three sensitivity experiments (the three rows following the "standard estimate") are about the impact of different data sets. In the 4th sensitivity study (4th row after "standard estimate"), the ratio of small mode AOD to total MODIS AOD was used for the anthropogenic fraction over the ocean

Table 2. Summary of the Global Annual Mean Anthropogenic Aerosol Forcing Estimates[a]

	TOA	Atmosphere	Surface
Standard estimate	−0.353 (W/m^2)	3.149	−3.513
1990-01 ISCCP + 2001-03 AERONET	−0.35	3.175	−3.533
1990-01 ISCCP + 1993-03 AERONET	−0.363	2.981	−3.343
without AERONET products	−0.258	3.28	−3.54
using MODIS small-mode AOD for anthropogenic fraction	−0.501	3.006	−3.514
all the aerosols trapped from surface to 1 km	−0.583	2.743	−3.338
all the aerosols are from 2 km to 4 km	−0.083	3.248	−3.341
Standard estimate without clouds	−1.08	3.42	−4.44

[a]Standard estimate above uses the 1999–2001 ISCCP data, 2001–2003 AERONET data, and the GOCART products for the anthropogenic fraction. However, we use the optimal mean over many experiments to present our best estimate values in the main text and Figure 8.

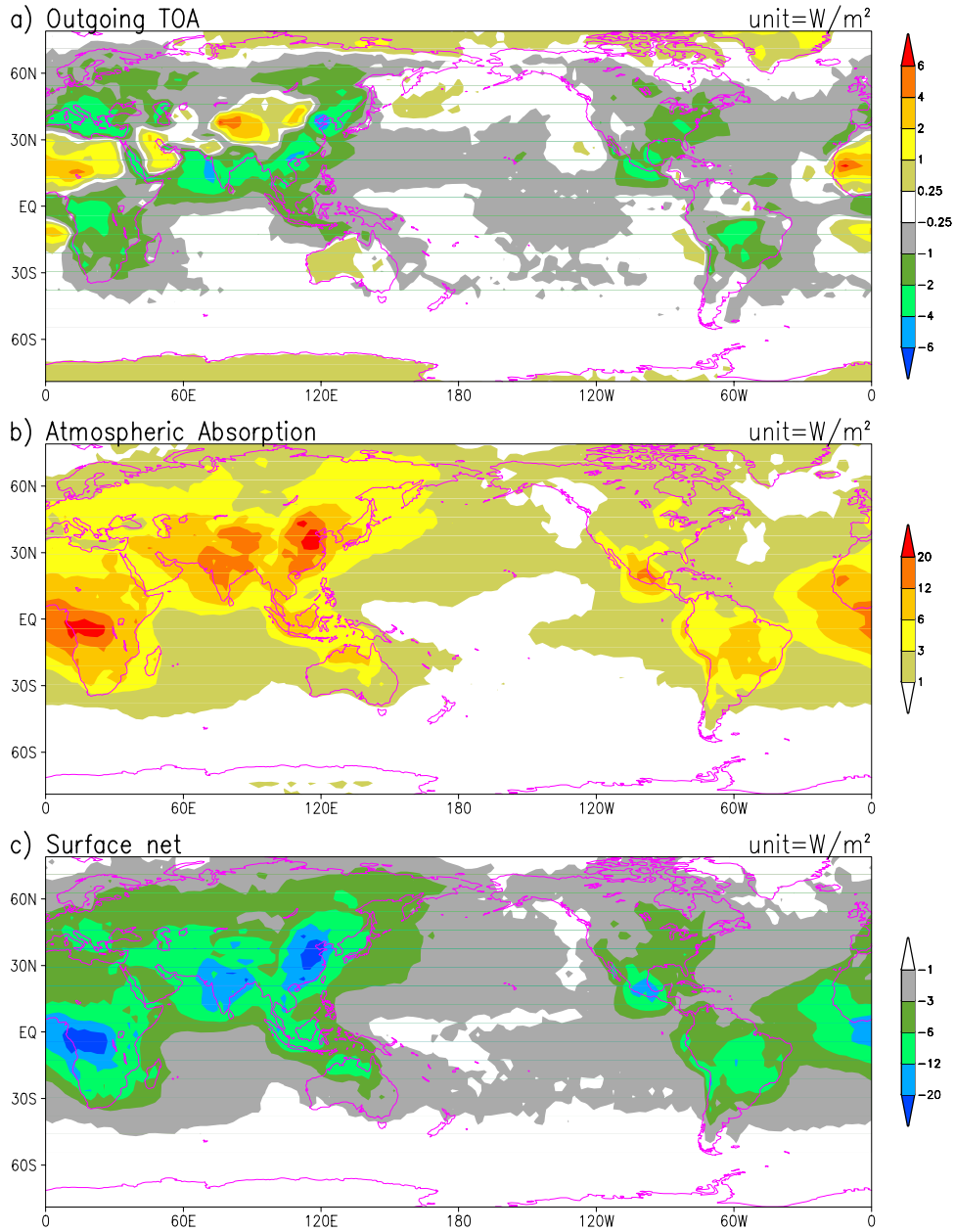

Figure 9. (a) Annual-mean anthropogenic aerosol forcing at the TOA. (b) Vertically integrated forcing in the atmosphere. (c) Forcing at the surface. The forcing calculation here includes cloud effects and uses integrated AODs, SSAs and asymmetry parameters with MODIS, GOCART and AERONET climatologies. The forcing in this figure is our standard and best estimate.

in place of the ratio derived from the GOCART simulated AODs. In the 5th and 6th experiments, the aerosol profiles were adjusted. The largest uncertainty is in the TOA forcing (Figure 8a and Table 2) which ranges by a factor of 6, from a large negative forcing of -0.6 Wm^{-2} to a negligible -0.1 Wm^{-2}, whereas the uncertainty in the surface is only about 10% and the atmospheric forcing uncertainty is of the order of 20%. Since the TOA forcing is the sum of the large positive atmospheric and the comparably large negative surface forcing, the roughly 10% to 20% uncertainties in these two terms translate into the factor of 6 uncertainty in the TOA forcing.

[48] The partitioning of the anthropogenic surface forcing in terms of the contribution from various regions of the planet to the global forcing is shown in Figure 8b. The NH land contributes the largest, about 36% to the total surface forcing, followed by aerosols over the NH ocean which contributes 28%; thus 64% of the total forcing is from the northern hemisphere. It should be noted that the forcing from NH oceans is, in reality, from aerosols transported mostly from NH land regions. The balance of 36% is from the southern hemisphere, out of which 21% is from the aerosols above the ocean and the balance of 15% from the SH land. The larger contribution from the SH ocean regions

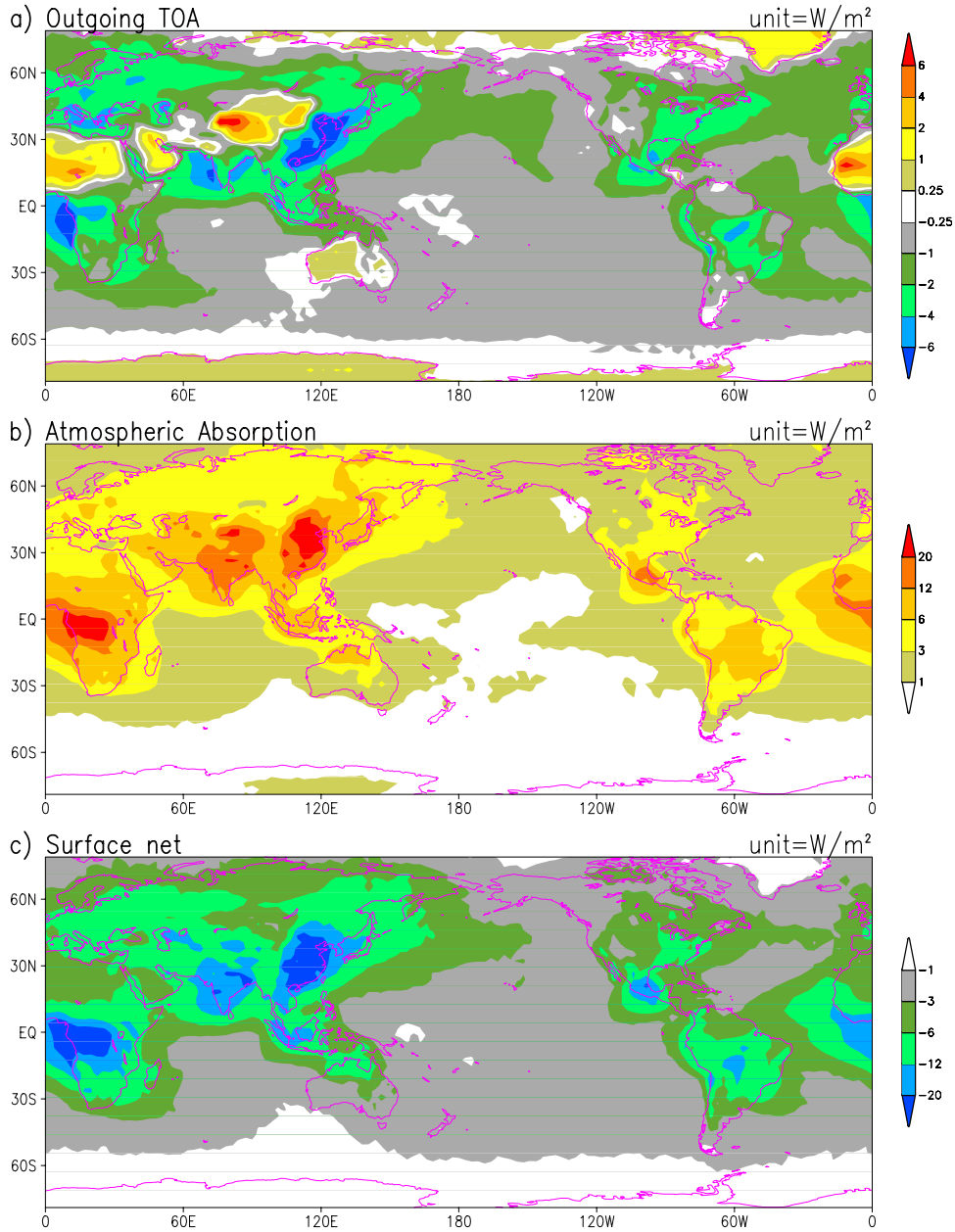

Figure 10. (a) Annual-mean anthropogenic aerosol forcing at the TOA. (b) Forcing in the atmosphere. (c) Forcing at the surface. The values in this figure are clear-sky forcing calculations and would otherwise be the same as Figure 9.

(compared with SH land regions) is simply due to the much larger fraction of the SH area covered by the ocean.

[49] We also show the surface forcing from the various continental sources. Asia and its nearby ocean contributes 34% of the global solar radiation reduction at the surface, and Africa and its nearby ocean ranks as the 2nd (28.5%).

[50] Reverting back to our best estimate, Figure 9 shows the global distribution of the anthropogenic aerosol forcing. The TOA forcing is generally negative except over the desert/ice areas where the surface albedo is high and the aerosol absorption of the solar radiation reflected from these bright surfaces overwhelms the scattering of solar radiation back to space. The areas with large atmospheric (>10 Wm^{-2}) and large negative surface forcing (<-10 Wm^{-2}) are eastern China, India, and equatorial Africa. Mexico and the Amazon area also have a significant amount of surface/atmosphere forcing. Clearly, the anthropogenic aerosol forcing is quite heterogeneous in space, pointing to its great potential in modulating the atmospheric circulation pattern.

[51] We re-ran the MACR model but without clouds and produced the clear-sky forcing as in Figure 10. The global mean forcing value is -1.08 Wm^{-2} (TOA), 3.42 Wm^{-2} (atmosphere) and -4.44 Wm^{-2} (surface), as in the last row of Table 2. Thus, removing clouds enhances the negative forcing at the surface by about 25% while the negative forcing at TOA is enhanced by nearly a factor of 2. The impact on the atmospheric forcing is only 10%. Clearly the

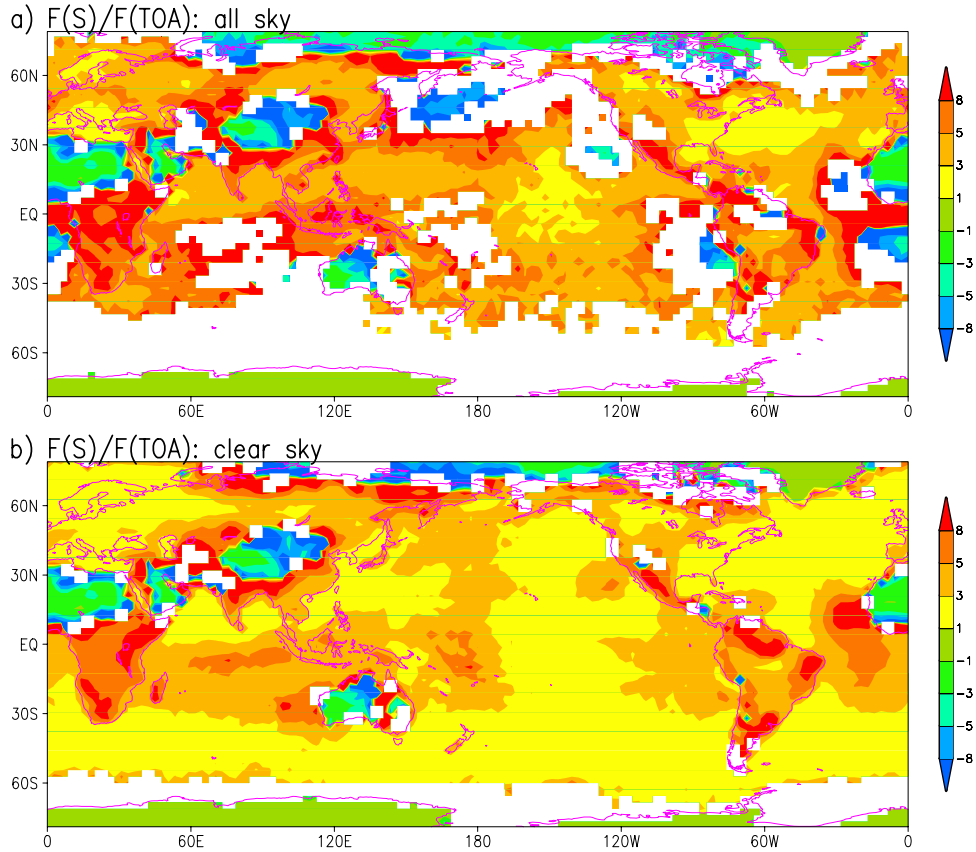

Figure 11. Ratio of aerosol forcing at surface [F(S)] to aerosol forcing at TOA [F(TOA)]. Again the annual-mean anthropogenic forcing is used. (a) Ratio in all skies. (b) Ratio in clear skies. The white shaded regions in the maps above indicate extremely low TOA forcing values close to zero and are usually associated with large ratios and have no physical significance. Aerosol forcing was calculated as in Figures 9 and 10.

main effect of clouds is to mask the effect of aerosols in reducing solar radiation at the surface [*Charlson et al.*, 1992] by as much as 0.9 Wm^{-2} (compare the top row with the bottom row of Table 2) and its effect on reducing atmospheric solar absorption (0.25 Wm^{-2}) is not as large. This is perhaps because the absorbing aerosols above clouds would absorb sunlight more due to those clouds and the absorbing aerosols below clouds would absorb less. On the contrary, the atmospheric forcing is very sensitive to the aerosol profile while the surface forcing is quite insensitive to the profile, as shown in Table 2.

[52] The all-sky regional forcing (Figure 9) patterns for the atmosphere and the surface are very similar to the clear-sky forcing (Figure 10) patterns. The TOA forcing, however, changes its sign from mostly negative values in clear skies to positive values in cloud skies over many regions. Those regions include the northern Pacific Ocean, the Atlantic adjacent to the southwestern Africa and the Pacific adjacent to South America.

[53] The ratio of surface forcing to TOA forcing is displayed in Figure 11. The ratio (Figure 11a) ranges from −8 to 8 over most of the oceanic and the land regions, revealing the dominance of the surface forcing over the TOA forcing. It should be noted that when TOA forcing is close to zero, the ratio can be much larger (see the white shaded regions in Figure 11) with very little physical relevance and hence we have masked these regions with a white shade. As described in *Ramanathan et al.* [2001], for strongly absorbing aerosols (SSA < 0.95) the surface forcing far exceeds the TOA forcing. Over high surface albedo land regions, the ratio changes sign into large negative values. This is because the TOA forcing becomes positive due to the increase in absorption of the reflected solar radiation. Extremely high ratios (both negative and positive) dominate polluted regions and their downwind areas around the world. The range of −8 to +8 for the surface to TOA forcing ratio may seem inconsistent with the roughly −10 ratio shown in Figure 8a for the global mean. This apparent inconsistency arises from the fact that the TOA forcing changes in sign, while the surface forcing is always negative. The results shown in Figures 9–11 clearly caution against relying solely on the global average TOA forcing to assess the climatic effects of aerosols.

[54] We would like to conclude by showing an example of the uncertainty in our estimates on regional scales. Figure 12 demonstrates the effects of including AERONET observations on the estimated forcing. In this figure, the atmospheric forcing averaged over South Asia (i.e., 60°–90°E and 5°–35°N mean) and that over East Asia (i.e., 100°–135°E and 25°–45°N mean) are displayed for 12 calendar months. As clear from this figure, the use of the AERONET observations adds noise (variations that may not

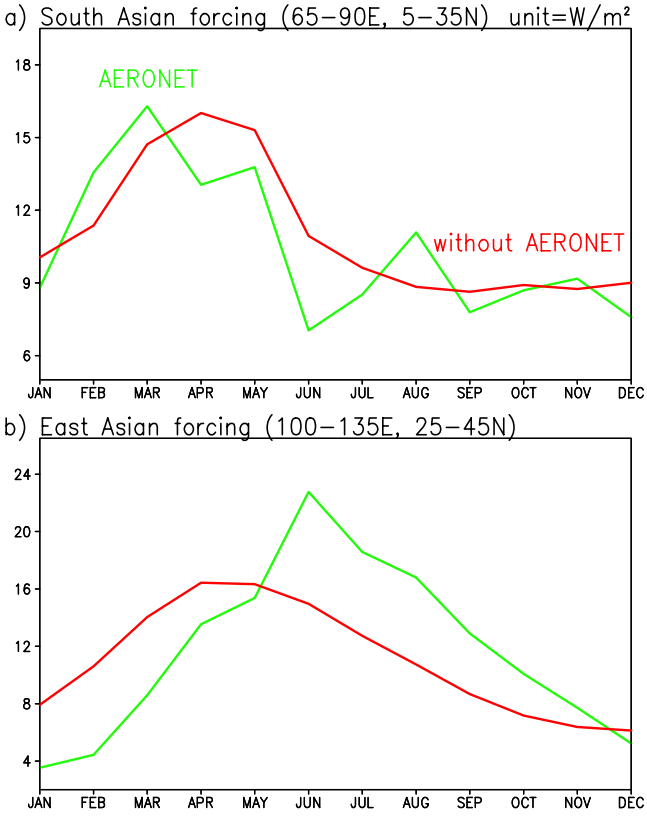

Figure 12. (a) Estimates of anthropogenic aerosol forcing in the atmosphere averaged over South Asia (60°−90°E and 5°−35°N). (b) Estimates over East Asia (100°−135°E and 25°−45°N). One estimate is the standard estimate (i.e., with AERONET), and the other is the estimate without AERONET observations.

be realistic) to the forcing, perhaps because of temporally-discontinuous AERONET data. In case of East Asia, adding the AERONET observations shifted the seasonal maximum of the aerosol loading estimates, suggesting usefulness of AERONET observation. The noise problem will be lessened as AERONET collects more data. Inclusion of data from other networks such as SKYradiometer NETwork (SKYNET [*Nakajima et al.*, 2003]) would also help.

6. Summary and Discussion

[55] In this study, we have estimated the direct effects of anthropogenic aerosols on solar radiation by integrating various products with the MACR model. The monthly climatology of AOD, SSA and asymmetry parameter was compiled by integrating MODIS, AERONET and GOCART products, and was employed into the MACR model. The cloud effects were addressed by adopting the ISCCP D2 product into MACR. Our study has derived the all-sky aerosol forcing over the entire globe mostly with observed aerosol properties. Most of the previous global aerosol forcing estimate studies were conducted with a CTM coupled to a GCM [e.g., *Hansen et al.*, 2002; *Takemura et al.*, 2002; *Wang*, 2004]. In such studies, errors are much larger because of the potentially larger deficiencies in simulating the distribution of the aerosol optical properties and the clouds. D. W. Fillmore et al. (Aerosol direct radiative forcing—Estimates from a global climatology constrained by MODIS assimilation, submitted to *Journal of Geophysical Research*, 2005) constrained their CTM-simulated aerosol by satellite aerosol observations. Their aerosol assimilation technique is another alternative to calculating the global forcing without being strongly influenced by uncertainties in aerosol emissions and their optical depths.

[56] Globally our study suggests that anthropogenic aerosols are strongly absorbing with SSA of about 0.85 to 0.88. The anthropogenic activities have enhanced global mean AODs by about 40% and the NH AODs by about 100%. Our best estimate of the global mean forcing given the uncertainty in this study is -0.35 Wm^{-2} at the TOA, $+3.0$ Wm^{-2} in the atmosphere and -3.4 Wm^{-2} at the surface. Our TOA estimate is close to the estimate at -0.19 Wm^{-2} by *Takemura et al.* [2002] and -0.65 Wm^{-2} by *Penner et al.* [1998].

[57] As our estimates show, because of the strongly absorbing nature of aerosols, the surface forcing is larger than the TOA forcing by a factor of about 10. Regionally, this ratio varies from -8 to $+8$, which may seem inconsistent with the global mean ratio of 10. This apparent inconsistency arises from the fact that the TOA forcing changes in sign while the surface forcing is always negative. Aerosols over the NH contribute about 64% to the total surface forcing. The uncertainties in the global atmospheric and surface forcing are less than 10−20%, whereas the uncertainty in the TOA forcing ranges six-fold from -0.6 Wm^{-2} to -0.1 Wm^{-2}. This is because the TOA forcing is a sum of the large positive atmospheric forcing and the comparably large negative surface forcing and small errors (of 10−20%) translate into a large uncertainty in the TOA forcing.

[58] Regionally the populated tropical regions contribute the most to the total surface forcing, with Asia the largest contributor. Furthermore the TOA forcing changes sign regionally and in addition, the ratio of surface to TOA forcing changes from strong positive values of 5 to 8 to strong negative values of -5 to -8. Thus caution must be exercised against relying too strongly on assessing the aerosol impacts based solely on global mean forcing.

[59] The present study has developed an independent approach for estimating anthropogenic aerosol forcing relying largely on observations. While satellite observations provide the backbone of the present estimates, surface network, i.e., AERONET, provided critical data to improve our estimates of aerosol optical properties.

[60] **Acknowledgments.** We thank two anonymous reviewers of an earlier version of this manuscript for their detailed comments which helped improve the presentation significantly. A portion of this work was conducted when one of us (V.R.) was a visiting scientist at the National Center for Atmospheric Research. We thank Dr. Li of Scripps Institution for graphic support; the Sounder Research Team (SRT) at the NASA Goddard Space Flight Center (GSFC) Laboratory for Atmospheres for providing the precipitable water data, and the AERONET support team for giving access to their data. In addition, we thank Dr. Yoram Kaufman for the MODIS data; Dr. Brent Holben for the AERONET data; and Dr. Mian Chin for the GOCART model output. This work was supported by a NSF grant (ATM-0201946) and a NASA grant (NNG04GC58G).

References

Barker, H. W., et al. (2003), Assessing 1D atmospheric solar radiative transfer models: Interpretation and handling of unresolved clouds, *J. Clim.*, *16*, 2676−2699.

Bond, T. C., D. G. Streets, K. F. Yarber, S. M. Nelson, J. Woo, and Z. Klimont (2004), A technology-based global inventory of black and organic carbon emissions from combustion, *J. Geophys. Res.*, *109*, D14203, doi:10.1029/2003JD003697.

Briegleb, B. P., P. Minnis, V. Ramanathan, and E. Harrison (1986), Comparison of regional clear-sky albedos inferred from satellite observations and model computations, *J. Clim. Appl. Meteorol.*, *25*, 214–226.

Charlson, R. J., et al. (1992), Climate forcing of anthropogenic aerosols, *Science*, *255*, 423–430.

Chen, T., W. B. Rossow, and Y. Zhang (2000), Radiative effects of cloud-type variations, *J. Clim.*, *13*, 264–286.

Chin, M., P. Ginoux, S. Kinne, O. Torres, B. N. Holben, B. N. Duncan, R. V. Martin, J. A. Logan, A. Higurashi, and T. Nakajima (2002), Tropospheric aerosol optical thickness from the GOCART model and comparisons with satellite and sunphotometer measurements, *J. Atmos. Sci.*, *59*, 461–483.

Chou, M.-D., P.-K. Chan, and M. Wang (2002), Aerosol radiative forcing derived from SeaWiFS retrieved aerosol optical properties, *J. Atmos. Sci.*, *59*, 748–757.

Chu, D. A., Y. J. Kaufman, C. Ichoku, L. A. Remer, D. Tanré, and B. N. Holben (2002), Validation of MODIS aerosol optical depth retrieval over land, *Geophys. Res. Lett.*, *29*(12), 8007, doi:10.1029/2001GL013205.

Clarke, A. D., et al. (2004), Size distributions and mixtures of dust and black carbon aerosol in Asian outflow: Physiochemistry and optical properties, *J. Geophys. Res.*, *109*, D15S09, doi:10.1029/2003JD004378.

Cooke, W. F., V. Ramaswamy, and P. Kasibhatla (2002), A general circulation model study of the global carbonaceous aerosol distribution, *J. Geophys. Res.*, *107*(D16), 4279, doi:10.1029/2001JD001274.

Cressman, G. P. (1959), An operational objective analysis system, *Mon. Weather Rev.*, *87*, 367–374.

Dubovik, O., B. N. Holben, T. F. Eck, A. Smirnov, Y. J. Kaufman, M. D. King, D. Tanre, and I. Slutsker (2002), Variability of absorption and optical properties of key aerosol types observed in worldwide locations, *J. Atmos. Sci.*, *59*, 590–608.

Eck, T. F., B. N. Holben, D. E. Ward, O. Dubovik, J. S. Reid, A. Smirnov, M. M. Mukelabai, N. C. Hsu, N. T. O'Neill, and I. Slutsker (2001), Characterization of the optical properties of biomass burning aerosols in Zambia during the 1997 ZIBBEE field campaign, *J. Geophys. Res.*, *106*, 3425–3448.

Eck, T. F., et al. (2005), Columnar aerosol optical properties at AERONET sites in central eastern Asia and aerosol transport to the tropical mid-Pacific, *J. Geophys. Res.*, *110*, D06202, doi:10.1029/2004JD005274.

Hansen, J., et al. (2002), Climate forcings in Goddard Institute for Space Studies SI2000 simulations, *J. Geophys. Res.*, *107*(D18), 4347, doi:10.1029/2001JD001143.

Hao, W. M., R. E. Babbitt, R. A. Susott, D. E. Ward, B. L. Nordgren, Y. J. Kaufman, B. N. Holben, and D. M. Giles (2002), Comparison of aerosol optical thickness measurements by MODIS, sun photometers, and haze-meters in Southern Africa during the SAFARI 2000 campaign, *Int. J. Remote Sens.*, *23*.

Harrison, E. F., P. Minnis, B. R. Barkstrom, V. Ramanathan, R. D. Cess, and G. G. Gibson (1990), Seasonal variation of cloud radiative forcing derived from the Earth Radiation Budget Experiment, *J. Geophys. Res.*, *95*, 18,687–18,701.

Haywood, J. M., and V. Ramaswamy (1998), Global sensitivity studies of the direct radiative forcing due to anthropogenic sulfate and black carbon aerosols, *J. Geophys. Res.*, *103*, 6043–6058.

Hess, M., P. Koepke, and I. Schult (1998), Optical properties of aerosols and clouds: The software package OPAC, *Bull. Am. Meteorol. Soc.*, *79*, 831–844.

Holben, B. N., et al. (2001), An emerging ground-based aerosol climatology: Aerosol optical depth from AERONET, *J. Geophys. Res.*, *106*, 12,067–12,097.

Huebert, B. J., T. Bates, P. B. Russell, G. Shi, Y. J. Kim, K. Kawamura, G. Carmichael, and T. Nakajima (2003), An overview of ACE-Asia: Strategies for quantifying the relationships between Asian aerosols and their climatic impacts, *J. Geophys. Res.*, *108*(D23), 8633, doi:10.1029/2003JD003550.

Jacobson, M. Z. (2001), Strong radiative heating due to mixing state of black carbon in atmospheric aerosols, *Nature*, *409*, 695–697.

Kaufman, Y. J., D. Tanré, L. A. Remer, E. Vermote, A. Chu, and B. N. Holben (1997), Operational remote sensing of tropospheric aerosol over land from EOS moderate resolution imaging spectroradiometer, *J. Geophys. Res.*, *102*, 17,051–17,067.

Kim, D.-H., B. J. Sohn, T. Nakajima, and T. Takamura (2005), Aerosol radiative forcing over East Asia determined from ground-based radiation measurements, *J. Geophys. Res.*, *110*, D10S22, doi:10.1029/2004JD004678.

Kinne, S., et al. (2003), Monthly averages of aerosol properties: A global comparison among models, satellite data, and AERONET ground data, *J. Geophys. Res.*, *108*(D20), 4634, doi:10.1029/2001JD001253.

Nakajima, T., et al. (2003), Significance of direct and indirect radiative forcings of aerosols in the East China Sea region, *J. Geophys. Res.*, *108*(D23), 8658, doi:10.1029/2002JD003261.

Payne, R. E. (1972), Albedo of the sea surface, *J. Atmos. Sci.*, *29*, 959–970.

Penner, J. E., R. Dickinson, and C. O'Neill (1992), Effects of aerosol from biomass burning on the global radiation budget, *Science*, *256*, 1432–1432.

Penner, J. E., H. Eddleman, and T. Novakov (1993), Towards the development of a global inventory of black carbon emissions, *Atmos. Environ, Part A*, *27*, 1277–1295.

Penner, J. E., C. Chuang, and K. Grant (1998), Climate forcing by carbonaceous and sulfate aerosols, *Clim. Dyn.*, *14*, 839–851.

Pincus, R., H. W. Barker, and J.-J. Morcrette (2003), A fast, flexible, approximate technique for computing radiative transfer in inhomogeneous cloud fields, *J. Geophys. Res.*, *108*(D13), 4376, doi:10.1029/2002JD003322.

Podgorny, I. A., and V. Ramanathan (2001), A modeling study of the direct effect of aerosols over the tropical Indian Ocean, *J. Geophys. Res.*, *106*, 24,097–24,105.

Podgorny, I. A., W. C. Conant, V. Ramanathan, and S. K. Satheesh (2000), Aerosol modulation of atmospheric and solar heating over the tropical Indian Ocean, *Tellus, Ser. B*, *52*, 947–958.

Ramanathan, V., R. D. Cess, E. F. Harrison, P. Minnis, B. R. Barkstrom, E. Ahmad, and D. Hartmann (1989), Cloud-radiative forcing and climate: Results from the Earth Radiation Budget Experiment, *Science*, *243*, 57–63.

Ramanathan, V., et al. (2001), The Indian Ocean Experiment: An integrated analysis of the climate forcing and effects of the Great Indo-Asian Haze, *J. Geophys. Res.*, *106*, 28,371–28,398.

Ramaswamy, V., et al. (2001), Radiative forcing of climate change, in *Climate Change 2001: The Scientific Basis*, by H. T. Houghton et al., chap. 6, pp. 349–416, Cambridge Univ. Press, New York.

Remer, L. A., et al. (2002), Validation of MODIS aerosol retrieval over ocean, *Geophys. Res. Lett.*, *29*(12), 8008, doi:10.1029/2001GL013204.

Reynolds, R. W. (1988), A real-time global sea surface temperature analysis, *J. Clim.*, *1*, 75–86.

Rossow, W. B., and R. A. Schiffer (1999), Advances in understanding clouds from ISCCP, *Bull. Am. Meteorol. Soc.*, *80*, 2261–2287.

Rossow, W. B., A. W. Walker, D. E. Beuschel, and M. D. Roiter (1996), International Satellite Cloud Climatology Project (ISCCP) documentation of new cloud data sets, p. 115.

Satheesh, S. K., V. Ramanathan, X.-L. Jones, J. M. Lobert, I. A. Podgorny, J. M. Prospero, B. N. Holben, and N. G. Loeb (1999), A model for the natural and antropogenic aerosols over the tropical Indian Ocean derived from Indian Ocean Experiment data, *J. Geophys. Res.*, *104*, 27,421–27,440.

Simmons, A. J., and J. K. Gibson (2000), The ERA-40 Project plan, *ERA-40 Proj. Rep. Ser.*, *1*, 63 pp.

Takemura, T., T. Nakajima, O. Dubovik, B. N. Holben, and S. Kinne (2002), Single-scatting albedo and radiative forcing of various aerosol species with a global three-dimensional model, *J. Clim.*, *15*, 333–352.

Tanré, D., Y. J. Kaufman, B. N. Holben, B. Chatenet, A. Karnieli, F. Lavenu, L. Blarel, O. Dubovik, L. A. Remer, and A. Smirnov (2001), Climatology of dust aerosol size distribution and optical properties derived from remotely sensed data in the solar spectrum, *J. Geophys. Res.*, *106*(D16), 18,205–18,217.

Vogelmann, A. M., V. Ramanathan, and I. A. Podgorny (2001), Scale dependence of solar heating rates in convective cloud systems with implications to General Circulation Models, *J. Clim.*, *14*, 1738–1752.

Wang, C. (2004), A modeling study on the climate impacts of black carbon aerosols, *J. Geophys. Res.*, *109*, D03106, doi:10.1029/2003JD004084.

C. E. Chung, D. Kim, I. A. Podgorny, and V. Ramanathan, Center for Clouds, Chemistry, and Climate (C^4), Center for Atmospheric Sciences, Mail #: 0221, Scripps Institution of Oceanography, 9500 Gilman Drive, La Jolla, CA 92093, USA. (cchung@fiji.ucsd.edu)